

Modeling of heterogeneous dustcake effect on particle migration of coal fly ash and PAC in a cylindrical ESP

Eric Monsu Lee^{1,*}, Herek L. Clack²

¹ Northern Illinois University, 104 Eng. Bldg., 590 Garden Road, DeKalb, IL 60115, USA

² University of Michigan, 169 EWRE Bldg., 1351 Beal Avenue, Ann Arbor, MI 48109, USA

* Corresponding author: elee3@niu.edu (Eric Monsu Lee)

Received: 13 July 2022

Revised: 1 November 2022

Accepted: 15 November 2022

Published online: 21 November 2022

Abstract

Powdered activated carbon (PAC) injection upstream of an electrostatic precipitator (ESP) has been the most mature mercury control technology at coal-fired power plants (CFPPs). However, the application of PAC injection showed increasingly darkened particulate matter (PM) samples collected from the stack emissions as the sorbent injection rate was increased. From our previous experimental study, the simultaneous precipitation of coal fly ash and PAC led to the formation of heterogeneous dustcake, with powder resistivity varying along the collection electrode. To study the mechanisms leading to the potential of particle penetration through ESPs during PAC injection, the present study aims to model the effect of heterogeneous dustcake in a cylindrical electrostatic precipitator (ESP) by developing a 2-D Euler-Lagrange numerical model. By prescribing a 2-D oscillatory boundary condition on the collection electrode, the results show that the presence of a heterogeneous dustcake can alter the electric field, ion density, and electrohydrodynamic (EHD) flow, characterized as a wave-like flow field, which is then shown to influence the particle trajectory length, particle charging rate, initial particle contact velocity, and particle collection efficiency.

Keywords: Coal-fired power plants, mercury sorbent injection, electrostatic precipitator model, heterogeneous dustcake resistivity, wave-like EHD flow field.

1. Introduction

Since April 2015, the Mercury Air Toxics Standards (MATS) promulgated by the U.S. Environmental Protection Agency (EPA) has been reinforcing the coal-fired power plants (CFPPs) to reduce their gaseous mercury emissions by 85-95% or 1.2 lb/TBtu. Injection of dried powdered sorbents such as powdered activated carbon (PAC) has been regarded as the leading control technology due to its prior successful applications at municipal and hazardous waste incinerators. However, it has been more challenging to implement PAC injection at CFPPs because the flue gas volumes that need to be treated are much greater than at the waste incinerators, leading to trace amounts of gaseous mercury that need to be adsorbed. PAC injection systems are commonly installed upstream of electrostatic precipitators (ESPs), which are widely used at approximately 90% of the CFPPs in the U.S., with 65% being implemented as the only particulate matter (PM) control device and 25% being utilized in combination with baghouses or fabric filters (FFs) [1, 2].

During PAC injection, one performance anomaly has been reported, which states that 15 the PM samples collected from the stack emissions become darkened as the sorbent injection rate increases [3, 4]. One hypothesis has been proposed and is related to the significant difference in electrical properties between coal fly ash and the commonly used carbon-based mercury sorbents with porous morphology and large specific surface area. It was hypothesized that the injection of PAC into the coal flue gas can induce unexpected particle migration behaviors for ESPs initially designed and operated for fly ash removal only. One of these unexpected collection behaviors is related to the formation of heterogeneous dustcake as particles with less electrical resistance (i.e., $10^4 \Omega\text{-cm}$) are collected at locations along the collection electrode different than the more resistive fly ash ($10^{12} \Omega\text{-cm}$) leading to the formation of dustcake with complex ring structures as shown in Fig. 1.

The effect of the collected dustcake on particle charging and collection in ESPs has been evaluated, centering on the phenomenon of back corona involving resistive dustcake. Back corona is a phenomenon referring to the generation of oppositely charged ions emitted from the resistive dustcake on the collection electrode. The polarity of the discharge electrode decides the type of ions emitted from the dustcake layers. If the discharge electrode has a negative polarity, the resistive dustcake emits negative ions during back corona and vice versa. These oppositely charged ions can neutralize the particle charging field composed of ions of single polarity and ultimately leads to quenching of corona discharge and reduction in particle collection efficiency. Previous experimental studies concerning back corona focused on the effect of humidity on the onset voltage of back corona [6], the various discharge forms involved during back corona [7], the effect of different gas compositions on back corona [8], the spectroscopic analysis of gaseous species emitted from dustcake during back corona discharge [7, 8], the characteristics of back corona under high temperatures [9] and the characterization of back corona from fly ash craters using particle image velocimetry (PIV) [10].

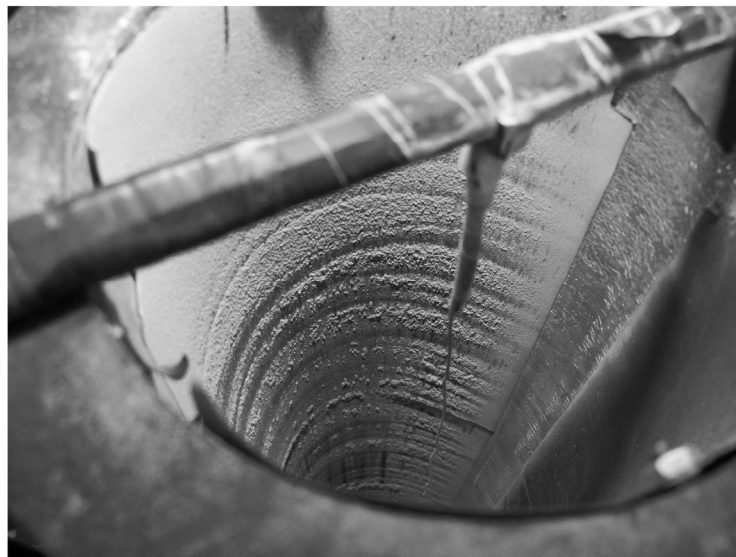


Fig. 1. Formation of complex and spatially varied dustcake structure as a result of feeding fly ash-PAC admixtures. [5]

The modeling of back corona typically involves solving the charge transport Eqs. for both negative and positive ions simultaneously with the Laplacian-Poisson electric field equation. Imposing distinctive boundary conditions enable the study of different features of back corona. Earlier works of modeling back corona primarily centered on developing different algorithms for solving the fully coupled charge transport and electric field equations. Lawless and Sparks [11] simulated different aspects of back corona based on voltage-current characteristics, current density distribution, and collection efficiency by using finite difference method. Hoburg [12] developed a back corona model to solve for the current density, electric field, and particle charges by defining a space charge density ratio between the positive and negative ion densities and compared the numerical results to the experimental data collected by Penny and Hewitt [13]. More recent modeling studies on back corona have focused on the effect of intrinsic properties of dustcake on the back corona characteristics. Bacchiega *et al.* [14] simulated the non-linear effects of dustcake resistivity and thickness by developing an electric circuit, considering the current densities of corona (forward) discharge through space and dustcake, and back discharge. Ivancsy *et al.* [15] defined an electric field intensity on the collection electrode and evaluated the effect of relative permittivity of dustcake on particle charging before collection and particle discharging after collection. Jansky *et al.* [16] incorporates surface charge density on dustcake into the Laplacian-Poisson electric field and charge transport equations to study the ignition of back corona from a micro sized pinhole located on the dielectric layer.

Very few studies from the past centered on the effect of dustcake heterogeneity with respect to composition and electrical properties on particle migration in ESPs. The effect of overall particle heterogeneity on particle migration in an ESP has been addressed in our previous studies [5], where the differential collection of fly ash and PAC admixtures with different mass concentrations were evaluated through electrostatic precipitation tests 64 through which the dustcake with complex ring structures was reported (Fig. 1).

The results from the electrostatic precipitation tests showed opposite trends in terms of two different coal fly ash admixtures. In Western Powder River Basin (WPRB) fly ash admixtures, the test results showed a reduction in overall particle collection efficiency and an increase in the mass of unaccounted for particles as the concentration of PAC was increased in the admixture. The mass of unaccounted for particles was defined as the particles mass that was not collected by the collection electrode. In other words, the mass of accounted for particles can include particle loss through particle penetration and to the non-collection electrode surfaces in the ESP [17]. In comparison, for admixtures composed of PAC and Illinois Bituminous fly ash, it led to opposite trends of increasing overall collection efficiency and reducing the mass of unaccounted for particles as PAC concentration was increased in the admixtures. The mass of unaccounted for particles for various PAC concentrations in the admixtures was non-negligible and even considered as significant for fly ash-PAC admixtures. The overall mass of unaccounted for particles when testing PAC-Illinois Bituminous fly ash admixtures reduced from 25 to 10 wt.% as PAC concentration was increased from 0–10 wt.%. In comparison, PAC-Western PRB fly ash admixtures only resulted in a relatively smaller variation in the total mass of unaccounted for particles, which ranged from 4 to 7 wt.%.

To infer the composition for the mass of unaccounted for particles and to study the dustcake heterogeneity, powder resistivity measurement was conducted on the powder samples collected from the collection electrode. Based on the percent difference in powder resistivity, the study concluded that as the concentration of less resistive PAC increased in the admixtures found on the collection electrode, the primary constituent of the unaccounted-for particles due to electrostatic precipitation can become increasingly more PAC-concentrated because the dustcake resistivity becomes more resistive. However, only the bulk resistivity of the collected dustcake was measured instead of measuring the differential powder resistivity along the collection electrode, and the effect of dustcake heterogeneity on particle migration was not studied explicitly.

The presence of dustcake without the onset of back corona has been determined to affect the particle migration behaviors in ESPs. Previous studies focused on the effect of thin dustcake with a thickness that ranged in between 0 and 5 mm. Gao *et al.* [18] developed a numerical model and looked at the effect of dustcake on the particle migration in a wire-plate ESP. The study concluded that thicker dustcake led to clear reduction in current density at a dustcake thickness of 3 to 5 mm. The reduction in current density led to the reduction in the electric field, particle charging rate, and the particle collection efficiency. Also, the study stated that dustcake resistivity has a greater impact on the collection of smaller particles with particle diameter less than or equal to 1 μm . Zheng *et al.* [19] conducted an experimental study and focused on comparing the discharge characteristics between stable discharge and back corona discharge under elevated gas temperatures up to 400 °C. The study concluded that higher gas temperatures coupled with thicker dustcake and smaller discharge gap can lower the onset voltage of back corona and thus, the electric field and the particle migration velocity when a dustcake with a high resistivity is present. Zhang *et al.* [20] developed a mathematical model to specifically study the effect of gas temperature on particle migration in a wire-plate ESP. The study concluded that higher gas temperature improved particle charging of smaller particles with low resistivity, but quenched particle charging of larger particles with high resistivity.

While the effect of dustcake on particle migration in an ESP has been studied without regarding back corona, the past studies only centered on the effect of homogeneous dust cake with uniformly distributed powder compositions. The effect of heterogeneous dustcake presents another case study in this field when PAC is injected upstream of an ESP to capture gaseous mercury. The injected PAC is precipitated simultaneously with the coal fly ash and can form dustcake with non-uniformly distributed composition. The present study aims to look at the effect of different forms of heterogeneous dustcake on the particle migration behaviors by developing a numerical model considering a lab-scale cylindrical ESP.

2. Numerical modeling of an ESP with a heterogeneous dustcake

The present numerical model was developed in COMSOL Multiphysics® v. 5.6. based on the sub-module of Particle Tracing for Fluid Flow [21]. Fig. 2 shows the Euler-Lagrange numerical scheme used in the present study. The operation of an ESP commonly involves mutually coupled physics that is usually initiated by first establishing an electric field responsible for perturbing the primary flow field with the electrohydrodynamic (EHD) secondary flow that in turn can affect particle migration behaviors. Consideration of particle charging kinetics further increases the complexity of ESP modeling, as particle charging typically involves time dependent diffusion and field charging. Two numerical schemes are commonly adapted for modeling the ESP,

including the Euler-Euler and Euler-Lagrange, with the latter being more computationally expensive but producing more reliable results [22].

2.1 Nonuniform electric field

The present study adapts the Euler-Lagrange scheme, which first solves the Eulerian variables, including the electric field (\vec{E}) and the ion concentration (ρ_{ion}), which are governed by the Laplacian-Poisson equation (Eq. 1) coupled with the charge transport equation (Eq. 2), where ϕ is the electric potential, \vec{J} is the current density, and K_{ion} is the ion mobility. Assuming an averaged inlet flow velocity of 0.1 m s^{-1} , the current density (\vec{J}) neglects ion convection and diffusive motion of ions and considers only the ionic current density in a cylindrical ESP [24].

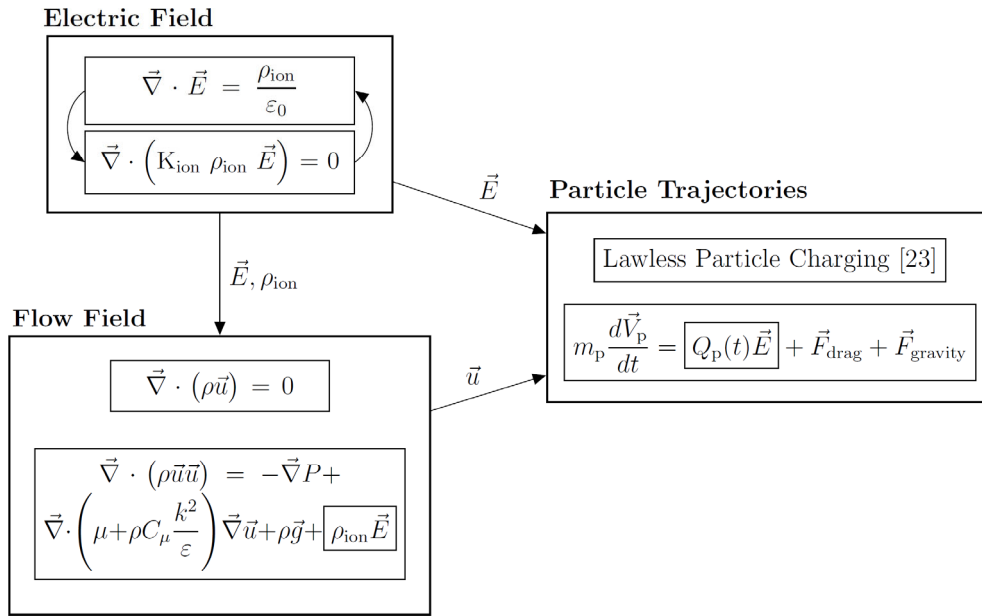


Fig. 2. multi-scale Euler-Lagrange numerical scheme for simulating the effect of heterogeneous dustcake.

The ion production/corona discharge is simulated based on Eq. 1 and Eq. 2, which are solved using the fully-coupled solver in COMSOL. Particle space charge density is neglected in Eq. 1 because the gas-solid flow is sparse, following the flow condition in our previous experimental study [5]. Ion production is controlled by the radius of discharge wire (r_c) in Eq. 19. Reducing the radius of wire can lead to higher ion concentration near the surface of the discharge wire.

$$\vec{\nabla} \cdot \vec{E} = \frac{\rho_{ion}}{\epsilon_0}; \quad \vec{E} = -\vec{\nabla} \phi \quad (1)$$

$$\vec{\nabla} \cdot \vec{J} = 0; \quad \vec{J} = K_{ion} \rho_{ion} \vec{E} \quad (2)$$

2.2 Electrohydrodynamic (EHD) flow

In an ESP, the nonuniform electric field and ion density near the discharge electrode lead to the formation of EHD secondary flow in addition to the primary gas flow. With the ion velocity on the order of 100 m s^{-1} [25], the fluid flow in an ESP is considered turbulent and is commonly modeled by the Reynolds-Averaged Navier-Stokes (RANS) equation coupled with the $k-\epsilon$ turbulent model in Eq. 3 [26, 27, 28]. The product of $\rho_{ion} \vec{E}$ serves as the volumetric force responsible for the formation of EHD flow.

$$\vec{\nabla} \cdot (\rho \vec{u}) = 0; \quad \vec{\nabla} \cdot (\rho \vec{u} \vec{u}) = -\vec{\nabla} P + \vec{\nabla} \cdot \left(\mu + \rho C_\mu \frac{k^2}{\epsilon} \right) \vec{\nabla} \vec{u} = + \rho \vec{g} + \rho_{ion} \vec{E} \quad (3)$$

2.3 Lagrangian particle tracing

To enable Lagrangian particle tracing, Newton's law is used as shown in Eq. 4, where \vec{U}_p is the particle velocity and the external forces affecting the velocity and position of a particle are imposed on the right hand side of the equation. The present study considers the time dependent electrostatic force, $\vec{F}_e(t)$, gravitational force, \vec{F}_g , and aerodynamic drag force, \vec{F}_d as these are the external forces that can significantly perturb the trajectories of particles in an ESP [29].

$$\rho_p V_p \frac{d\vec{U}_p}{dt} = \vec{F}_g + \vec{F}_e(t) + \vec{F}_d \quad (4)$$

The gravitational force, \vec{F}_g is defined in Eq. 5, where ρ_f is the gas density. The electrostatic body force is the product of a time dependent particle charge, $Q_p(t)$ and the electric field, \vec{E} where the time dependent particle charge is the product of an elementary charge (e) and the time dependent electric charge number ($Z(t)$), which increases as each particle traverses the electrostatic column. The time dependent particle charge is modeled by the particle charging kinetics developed by Lawless [23], which is defined by Eq. 7.

$$\vec{F}_g = \left(\frac{\rho_p - \rho_f}{\rho_p} \right) m_p \vec{g} \quad (5)$$

$$\vec{F}_e(t) = Q(t) \vec{E} = eZ(t) \vec{E} \quad (6)$$

Eq. 7 describes the dimensionless rate of particle charging ($\tau_c dZ/dt$), where τ_c in Eq. is the characteristic particle charging time used for normalizing the total particle charging rate (dZ/dt), R_f (Eq. 9) and R_d (Eq.10) are, respectively, the dimensionless rates responsible for field and diffusion charging, and f_a (Eq. 11) is a coupling function connecting between the two charging kinetics.

$$\tau_c \frac{dZ}{dt} = \begin{cases} R_f + f_a & , (|v_e| \leq |v_s|) \\ R_d f_a & , (|v_e| > |v_s|) \end{cases} \quad (7)$$

In Eq. 8, ρ_i is the space charge density, μ is the ion mobility, k_B is the Boltzmann constant, and T_i is the ion temperature. In Eq. 9 and Eq.10, v_e indicates the dimensionless particle charge and v_s is the dimensionless saturation charge for each particle, where ϵ_r is the relative permittivity of the particle. In Eq.11, the join function depends on a normalized electric field (ω_e), which is defined in Eq. 12, where d_p is the particle diameter.

$$\tau_c = \frac{e^2}{4\pi\rho_i\mu k_B T_i} \quad (8)$$

$$R_f = \frac{v_s}{4\epsilon_0} \left(1 - \frac{v_e}{v_s} \right)^2 \quad (9)$$

$$R_d = \frac{v_e - v_s}{\exp(v_e - v_s) - 1} \quad (10)$$

$$f_a = \begin{cases} \frac{1}{(\omega_e + 0.475)^{0.575}} & , (\omega_e \geq 0.525) \\ 1 & , (\omega_e < 0.525) \end{cases} \quad (11)$$

$$\omega_e = \frac{e d_p |E|}{k_B T_i} \quad (12)$$

Following Eq. 7, neutralized particle suspensions ($v_e = 0$) start to accumulate electric charges as soon as they enter the charging domain. Initially, each particle obtains electric charge through field charging (R_f), if the total charge (v_e) is less than its saturation charge (v_s). If v_e exceeds its saturation limit, v_s , field charging

terminates and diffusion charging kinetics (R_d) becomes the only particle charging mechanism until the particle is collected. In a typical ESP, a particle can reach its saturation charge within a second, while the particle continues to obtain charges slowly through diffusion charging. The rate of diffusion charging decreases as a particle obtains more charges beyond its saturation level.

$$v_e = \frac{Ze^2}{2\pi\epsilon_0 d_p k_B T_i} \quad (13)$$

$$v_s = 3\omega_e \frac{\epsilon_r}{\epsilon_{r+2}} \quad (14)$$

2.4 Haider-Levenspiel drag law

In Eq. 4, the drag force, \vec{F}_d experienced by each particle flux is modeled by the Haider-Levenspiel drag law to account for the wide particle sizes and the non-sphericity of PAC. In general, the drag force is computed following Eq. 15, where τ_p is the particle velocity response time depending on the drag law used and C_c is the Cunningham correction factor defined by Eq. 16, where K_n is the Knudsen number depending on mean free path of gas (λ) and particle diameter (d_p). Eq. 17 shows the particle response time for the Haider-Levenspiel drag law. The response time is a function of drag coefficient (C_D), relative Reynolds number (Eq. 18) and empirically derived coefficients [30].

$$\vec{F}_d = \frac{1}{\tau_p C_c} m_p (\vec{u} - \vec{U}_p) \quad (15)$$

$$C_c = 1 + K_n [2.34 + 1.05 \exp(-\frac{0.39}{K_n})]; \quad K_n = \frac{\lambda}{d_p} \quad (16)$$

$$\left\{ \begin{array}{l} \tau_p = \frac{4\rho_p d_p^2}{3\mu C_D Re_r} \\ C_D = \frac{24}{Re_r} [1 + A Re_r^B] + \frac{C}{1 + \frac{D}{Re_r}} \end{array} \right. ; Re_r = \frac{\rho \|\vec{u} + \vec{U}_p\| d_p}{\mu} \quad (17)$$

$$Re_r = \frac{\rho \|\vec{u} - \vec{U}_p\| d_p}{\mu} \quad (18)$$

2.5 Boundary conditions

Table 1 summarizes the boundary conditions for solving the Eulerian variables, which are subsequently used for simulating the particle trajectories of fly ash and PAC. For the electric potential, a Neumann boundary value of E_0 is prescribed at the discharge electrode. The E_0 describes a constant electric field based on the Kaptsov's hypothesis [31] and is calculated by Peek's semi-empirical formula in Eq. 19, where r_c is the radius of the ionization zone, α is the surface roughness of the discharge wire, and δ is the relative density of air, defined by pressure (P) and temperature (T) in Eq. 20.

$$E_0 = 3.1 \times 10^6 \alpha \delta [1 + \frac{0.0308}{\sqrt{\delta r_c}}] \quad (19)$$

$$\delta = (\frac{293}{273+T}) (\frac{P}{101325}) \quad (20)$$

To model the effect of heterogeneous dustcake on particle trajectories, a two dimensional voltage drop ($\Delta V(r, z)$) is prescribed on the collection electrode. The voltage drop across the dustcake is defined in Eq. 21, where ρ_v is the dustcake resistivity, J is the instantaneous current density, and h is the dustcake thickness. The heterogeneous dustcake used in the present study assumed a constant dustcake thickness of 1 mm with the powder resistivity varied along the collection electrode. This is because for a dustcake thickness greater than 1 mm, the reduction in the particle charging field because of a homogeneous dustcake decays exponentially to a plateau [32].

Table 1. Boundary conditions at the inlet, outlet, collection electrode (CE) and discharge electrode (DE) for solving the Eulerian variables, including the electric potential, ϕ , ion space charge density, ρ_{ion} , EHD flow field, u .

Variables	Inlet	Outlet	CE	DE
ϕ	$\frac{\partial \phi}{\partial n} = 0$	$\frac{\partial \phi}{\partial n} = 0$	$\phi = \Delta V(r, z)$	$\frac{\partial \phi}{\partial n} = -E_0$
ρ_{ion}	$\frac{\partial \rho_{ion}}{\partial n} = 0$	$\frac{\partial \rho_{ion}}{\partial n} = 0$	$\frac{\partial \rho_{ion}}{\partial n} = 0$	$\rho_{ion} = \rho_{tm}$
u	0.1 (m s ⁻¹)	$P = P_{atm}$	$\frac{\partial u}{\partial n} = 0$	$\frac{\partial u}{\partial n} = 0$

$$\Delta V(r, z) = \rho_v(z)J(r, z)h \quad (21)$$

The present model assumes a mean gas velocity of 0.1 m s⁻¹ in the cylindrical ESP. The operation of an industrial ESP involves a gas flow with a velocity ranging from 0.5–2 m s⁻¹ for a wire-plate ESP and a much lower flow velocity for a cylindrical ESP depending on the total gas flow rate [33]. As a result, a lower mean gas flow velocity is imposed at the inlet and a pressure constraint of one atmosphere pressure is used for solving the EHD flow field in Table 1.

2.6 Particle properties

Table 2 shows the particle properties of fly ash and PAC used in the present model. Four discrete particle sizes for PAC are chosen in that they represent a realistic range of particle size distribution for PAC. On the other hand, fly ash has a wider particle size distribution, but to study the effect of powder heterogeneity on the ESP collection behaviors, an identical set of particle sizes was chosen here. Measured in our previous study, the bulk density of fly ash is approximately three times denser than that of PAC and the powder resistivity of fly ash is about eight orders of magnitude greater than PAC [5]. In addition, Table 3 indicates the rate of particle numbers introduced into the numerical domain for fly ash and PAC assuming four discrete particle sizes. To simulate the effect of heterogeneous dustcake on particle trajectories, the model assumes the mass flow rates for fly ash and PAC at 1 mg s⁻¹ and 0.1 mg s⁻¹ respectively. Noticeably, the number of fly ash particles introduced is approximately one order of magnitude greater than PAC.

The physical and electrical properties of fly ash and PAC differ greatly from each other. Except for having a porous structure, PAC is also considered non-spherical, so a sphericity of 0.7 is assumed [34]. Dielectric constant is important in particle charging as it defines the maximum charging capacity a particle can acquire through field charging. The dielectric constant of fly ash is significantly greater than PAC. A previous study showed that the dielectric constant of fly ash can be as high as 10⁴ [35], while the dielectric constant of PAC is approximated as black carbon at five [36].

The dielectric constant can affect the particle velocity significantly after particle charging in an ESP. A large dielectric constant for fly ash indicates almost instant particle collection with a particle collection time in the order of ms, while a smaller dielectric constant for PAC allows for longer particle trajectories before particle collection. This means that actual particle collection of fly ash will be more concentrated in the first collection field of the cylindrical ESP in Fig. 18. During numerical modeling, a large dielectric constant requires a smaller time step in the order of 10⁻⁴ s to capture the fast acceleration of particles with large dielectric constant, but small time stepping can also lead to unrealistic computation time. As a result, a smaller dielectric constant of 50 is adapted for fly ash for efficient convergence of the solutions for fly ash.

2.7 Numerical procedure

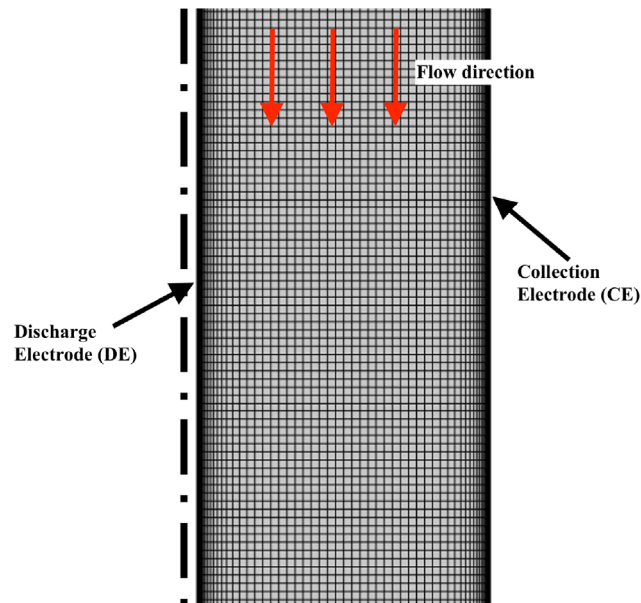
The present model follows a numerical solution sequence of first solving the stationary electric field, \vec{E} and ion density, ρ_{ion} . The solutions from the Laplacian-Poisson equations are used for solving the EHD secondary flow field in a mean gas flow of 0.1 m s⁻¹ by imposing the volumetric force of $\rho_{ion}\vec{E}$. The particle trajectories are solved using the previously computed \vec{E} , transient particle charge $Q_p(t)$, and flow field \vec{u} following an one-way coupling approach by assuming a dilute flow.

Table 2. Physical and electrical properties of fly ash and PAC used in the present model.

Particle properties	Fly ash	PAC
Bulk density (g cc ⁻¹)	1	0.3
Sphericity	1	0.7
Dielectric constant	50	5
Resistivity (Ω-cm)	10 ¹²	10 ⁴
Particle size (μm)	0.1, 1, 10, 100	0.1, 1, 10, 100

Table 3. Rate of number of particles introduced at the inlet of the cylindrical ESP for the four particle sizes assuming a mass flow rate of 1 mg s⁻¹ for fly ash and 0.1 mg s⁻¹ for PAC.

Particle properties	Fly ash (# s ⁻¹)	PAC (# s ⁻¹)
0.1	2 × 10 ²⁴	2 × 10 ²³
1	2 × 10 ²¹	2 × 10 ²⁰
10	2 × 10 ¹⁸	2 × 10 ¹⁷
100	2 × 10 ¹⁵	2 × 10 ¹⁴

**Fig. 3.** The axisymmetric mesh generated in the present study using a mapped mesh with a boundary layer mesh near the discharge and collection electrodes with a total of 27,180 domain elements and 1,026 boundary elements. The discharge electrode has a diameter of 1/16" (1.6 mm) and the collection electrode has a diameter of 5.75" (150 mm) with both electrodes having a total length of 36" (900 mm).

2.8 Meshing

A mapped mesh is generated for the axisymmetric domain having a length a 900 mm and a radius of 150 mm. Mesh refinement is achieved by using a boundary layer mesh to account for the larger gradients in ion density and electric field near the discharge electrode. Boundary layer mesh is also used near the collection electrode to reveal the effect of heterogeneous dustcake near the collection electrode. Fig. 3 shows the optimized mapped mesh with finer elements near the discharge and collection electrodes. There are a total of 27,180 domain elements and 1,026 boundary elements. The present mesh is optimized based on a mesh independence study conducted previously [17].

3. Results and discussion

During the electrostatic precipitation testing of two different fly ash-PAC admixtures, it was observed that the addition of PAC can lead to the formation of complex dustcake structures as shown in Fig. 1 [5]. One explanation for the formation of such dustcake structure is because fly ash is much more resistive than PAC. As a result, the particle migration characteristics of PAC can be different than fly ash after reaching different charge states leading to the formation of heterogeneous dustcake with dustcake resistivity varying along the collection electrode.

Dustcake resistivity varying along the collection electrode is modeled by using a periodic function. Eq. 22 defines a cosine function imposed on the collection electrode, where n indicates the dustcake varying frequency, L_c is the length of collection electrode, R_c is the radius of the collection electrode, $\rho_{v,FA}$ is the fly ash resistivity and $\rho_{v,PAC}$ is the PAC resistivity. The use of such a periodic function is to examine solely the effect of dustcake resistivity varying along the collection electrode while holding the dustcake thickness constant at 1 mm in Eq. 21. The choice of a cosine function is primarily for more efficient numerical convergence such that a nonzero value in dustcake resistivity is present on the collection electrode near the ESP inlet.

$$\rho_v(z) \Big|_{r=R_c} = \left[\rho_{v,FA} \cos \left[\frac{2n\pi}{L_c} z \right] \right] + \rho_{v,PAC} \quad (22)$$

In Eq. 22, the dustcake resistivity varying frequency, n defines how frequently the powder resistivity is varied in between the powder resistivity values of fly ash and PAC on the collection electrode. Fig. 4 indicates the current density as a function of n and axial location, z along the collection electrode. As shown in the Fig., the change in n can result in nonuniform distribution of current density. Based on conservation of electric charge, increasing the dustcake resistivity varying frequency leads to reduction in maximum current density through the dustcake, but results in negligible effect for small current density.

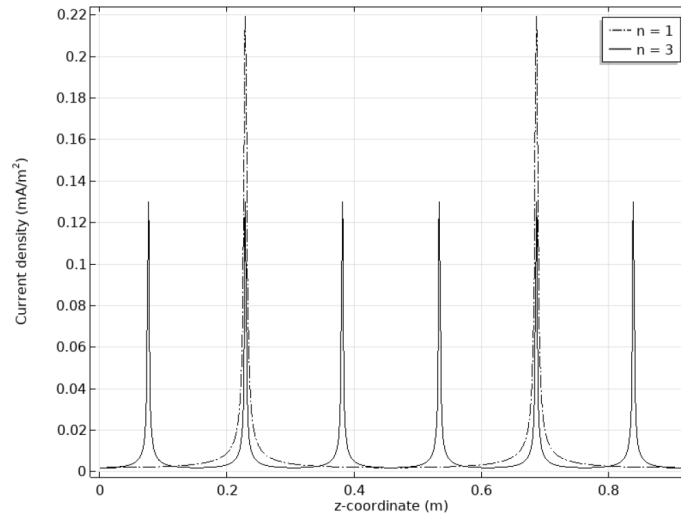


Fig. 4. The resultant current density spatially varied along the collection electrode under different powder resistivity varying frequencies (n).

3.1 Model validation vs. experimental data

Fig. 5 shows current density as a function of discharge voltage compared between the present study based on a cylindrical ESP and studies conducted by Gao *et al.* based on a wire-plate ESP [18]. In Fig. 5 (a), the dashed line represents the case of homogeneous dustcake with a dustcake thickness of 1 mm, which fits accurately into the lower end of Fig. 5 (b) when the discharge voltage is less than 40 kV. This result serves as a further validation of the numerical model developed in the present study. Also, Fig. 5(a) shows the effect of heterogeneous dustcake on the current density as the discharge voltage increases. As n increases, current density first increases at $n = 1$ and $n = 2$ but decreases at $n = 3$. This trend could be a result of reduction in dustcake heterogeneity as n increases.

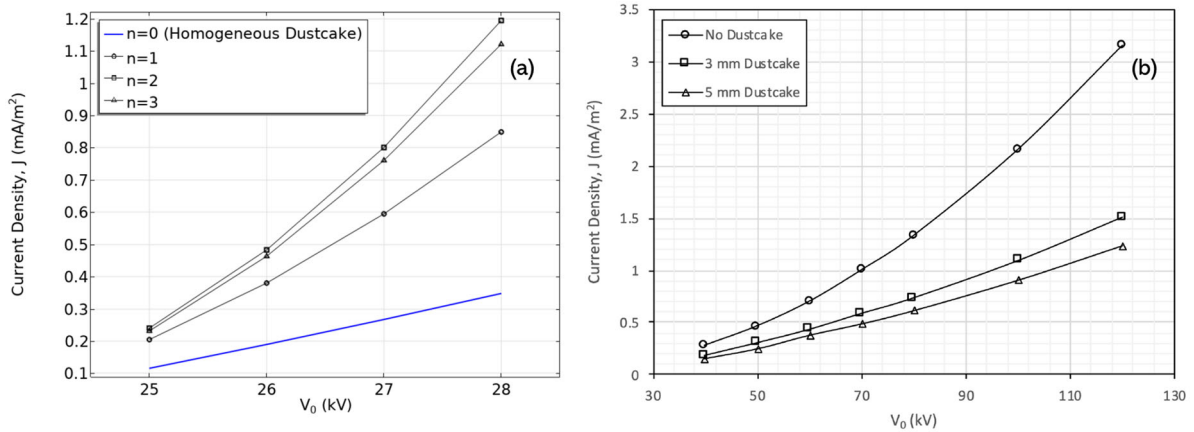


Fig. 5. Current density plotted as a function of discharge voltage and dustcake type, compared between (a) the present modeling study based on a cylindrical ESP and (b) the experimental study based on a wire-plate ESP [18].

3.2 Varying dustcake resistivity induced electric field

The effect of dustcake resistivity varying frequency (n) can potentially be explained based on particle aggregation on a charged surface [37]. Fig. 6 shows the sketch of induced axial and radial electric fields as a result of dustcake resistivity varying frequency. In the Fig., each curve represents the change in dustcake resistivity along the collection electrode by assuming a constant dustcake thickness of 1 mm. In Fig. 6, ΔV_1 and ΔV_3 represent voltage drops at crest locations where dustcake resistivity reaches a local maximum and current density reaches a local minimum. ΔV_2 and ΔV_4 represent voltage drops at trough locations where dustcake resistivity reaches a local minimum and current density reaches a local maximum.

Due to conservation of electric charge, the peak current density based on a higher dustcake resistivity varying frequency (i.e., $n = 3$) is smaller than the peak current density due to a lower value of n . In dustcake regions of higher resistivity, the voltage drop (ΔV) is higher and vice versa. To further this discussion, Fig. 6 shows the schematic of two hypothetical dustcake defined by two different resistivity varying frequencies and indicates the induced radial and axial electric fields.

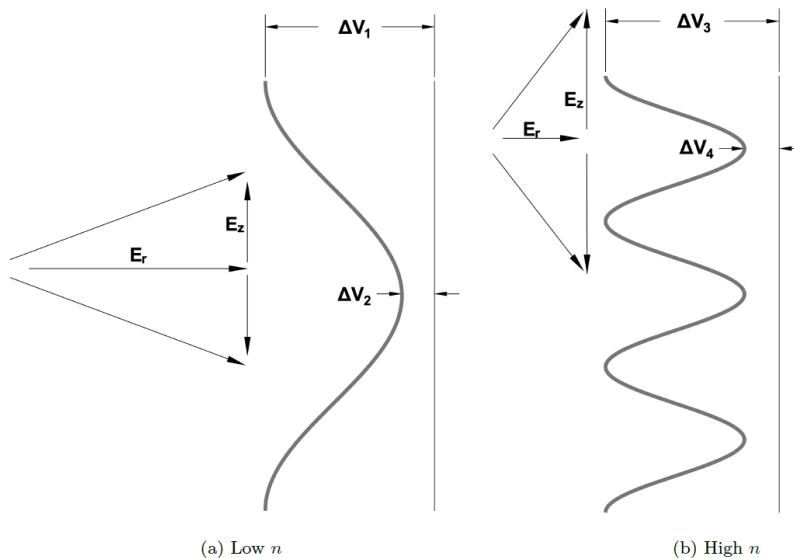


Fig. 6. The sketch showing the radial and axial electric fields due to the effect of increasing dustcake resistivity varying frequency (n) in powder resistivity with the vertical line to the right indicating the collection electrode.

In Fig. 6, ΔV_4 is always less than ΔV_2 , resulting in a stronger electric field in the radial direction, E_r for smaller n dustcake. In addition, ΔV_1 is equal to ΔV_3 assuming the minimum current density is approximately identical as shown in Fig. 4. Further, in Fig. 6, the resulting electric field in the axial direction, E_z also depends

on n . The difference between voltage drops is greater for the case of higher n , $(\Delta V_3 - \Delta V_4) > (\Delta V_1 - \Delta V_2)$ and the axial distance between the crest and the trough is smaller, resulting in a higher axial electric field ($E_z = dV/dz$) for larger n . Therefore, larger n dustcake can induce a stronger axial electric field that points either upward or downward and could alter the particle migration leading to the potential of particle penetration, especially for dustcake formed in the last collection field of an ESP.

3.3 Effect of varying dustcake resistivity on electric field

Fig. 7 shows the effect of dustcake varying frequency (n) on the electric field. The model dustcake with powder resistivity varied on the collection electrode creates distortions on the electric field lines near the collection electrode surface. Qualitatively, the electric field lines become sectioned as n increases with the electric field lines converging to regions, where the powder resistivity is minimal nearing the value of PAC. Quantitatively, the maximum (-5.4 MV m^{-1}) and minimum (-0.12 MV m^{-1}) electric field strength remain unaffected as n increases.

The contours of the electric field can affect ion transport and therefore particle charging. As generated ions are accelerated toward the collection electrode by the nonuniform electric field. It is known that the ion trajectories should be everywhere perpendicular to the electric field lines and the subsequent ion-particle collisions can lead to particle drifting toward the collection electrode. The increasing number of converging regions on the collection electrode due to the oscillatory dustcake implies that the particle fluxes approaching the regions of minimal resistivity are transported either upward or downward toward the collection electrode forming the complex ring dustcake on the collection electrode (Fig. 1).

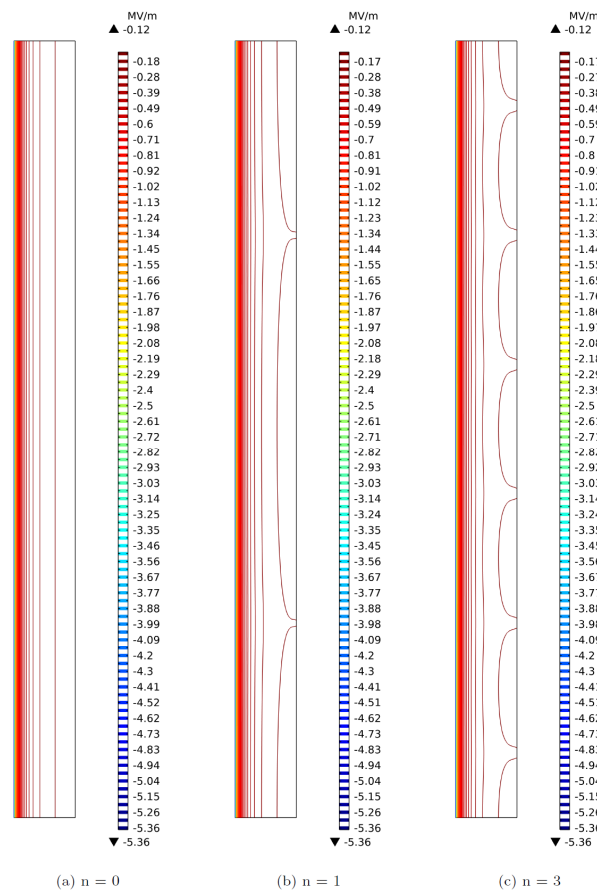


Fig. 7. Distortion of electric field lines by a heterogeneous dustcake with powder resistivity varied along the collection electrode modeled by using a dustcake thickness of 1 mm, a discharge voltage of -25 kV , and a mean flow velocity of 0.1 m s^{-1} .

3.4 Effect of varying dustcake resistivity on ion density

Fig. 8 shows the effect of heterogeneous dustcake on the distribution of ion density, which plays an essential

role in the rate of particle charging and generation of EHD secondary flow. For a homogeneous dustcake, ion density is only a function of radial coordinate (r) that varies between 5.71 and $7.83 \mu\text{C m}^{-3}$ as predicted by the model. On the contrary, a heterogeneous dustcake can induce significant changes to the distribution of ion density. Fig. 8 (b) and Fig. 8 (c) show the changes in ion density as the hypothesized dustcake varying frequency (n) increases from 1 to 3. Clearly, a heterogeneous dustcake leads to the formation of localized distribution of ion density with maximum ion density appearing at locations near the discharge electrode and decaying radially outward into the inter-electrode space. As n increases, the maximum localized ion density decreases, for example, $10.8 \mu\text{C m}^{-3}$ ($n = 1$) and $9.03 \mu\text{C m}^{-3}$ ($n = 3$) as predicted by the model.

A heterogeneous dustcake can alter the particle charging mechanisms in an ESP because of the localized ion density distribution. It is known that ion density affects the rate of particle charging with respect to both diffusion and field charging [38]. In Fig. 8, a dustcake with $n = 1$ induces two localized ion density zones and a dustcake with $n = 3$ induces six localized ion density zones. These zones can lead to inhomogeneous particle charging and particle collection. For a particle flux that interacts with one of the localized charging zones, two collection behaviors can take place: first, if the particle experiences maximum charging, it should be collected at a location opposite the region with maximum ion density, and second, if a particle experiences minimum particle charging, it can follow an oscillatory trajectory prior to particle collection or particle penetration. Also, a localized ion density zone can increase dustcake heterogeneity because particles of both types that possess higher saturation charges can readily be collected at the location opposite the maximum ion density. This not only increases the heterogeneity of the dustcake, but also the thickness of the dustcake at the location. Uneven dustcake thickness can lead to premature particle reentrainment due to the initially planned electrode rapping frequency.

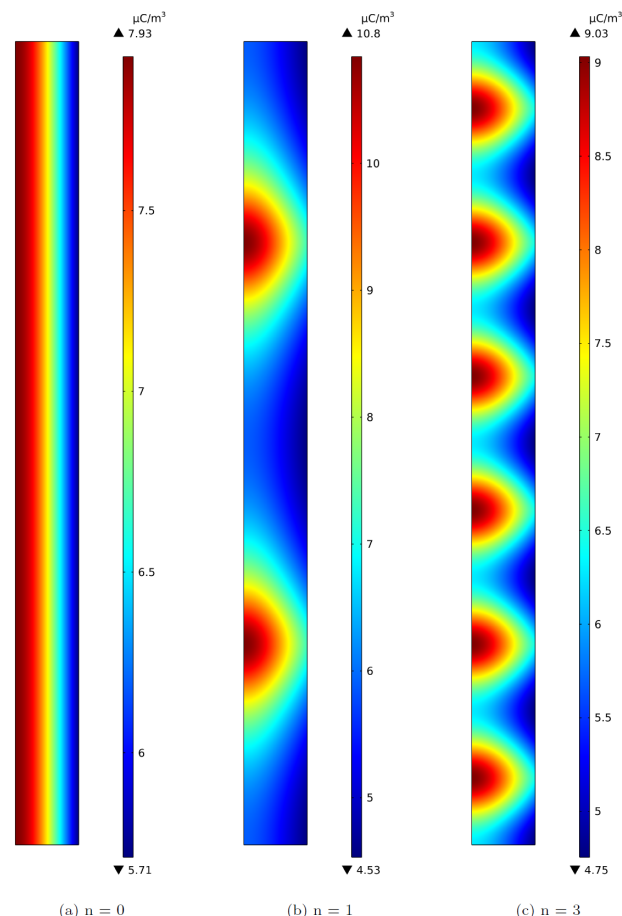


Fig. 8. Development of localized ion density distribution as a result of heterogeneous dustcake at different dustcake varying frequency (n) based on a constant dustcake thickness of 1 mm and a discharge voltage of -25 kV.

3.5 Varying dustcake resistivity effect on EHD flow

The product of ion density and electric field (i.e., $\rho_{ion} E_i$) produces a volumetric force known to perturb the

primary flow field, generating a secondary EHD flow field. Fig. 9 shows the effect of heterogeneous dustcake resistivity on the model-predicted EHD flow field, indicated by the color plot and the corresponding streamlines. In the present model, a mean fluid velocity of 0.1 m s^{-1} is assumed to simulate the flow condition in the cylindrical ESP operated at a discharge voltage of -25 kV . In Fig. 9 (a), the streamlines are unperturbed due to a homogeneous dustcake. In Fig. 9 (b), at $n = 1$, a clear wave-like flow field is induced as a result of the oscillatory dustcake. The presence of the heterogeneous dustcake pushes the streamlines away at collection electrode locations where the powder resistivity is minimal or where the less resistive PAC is collected. As n increases, both the wavelength and amplitude of the streamlines decrease

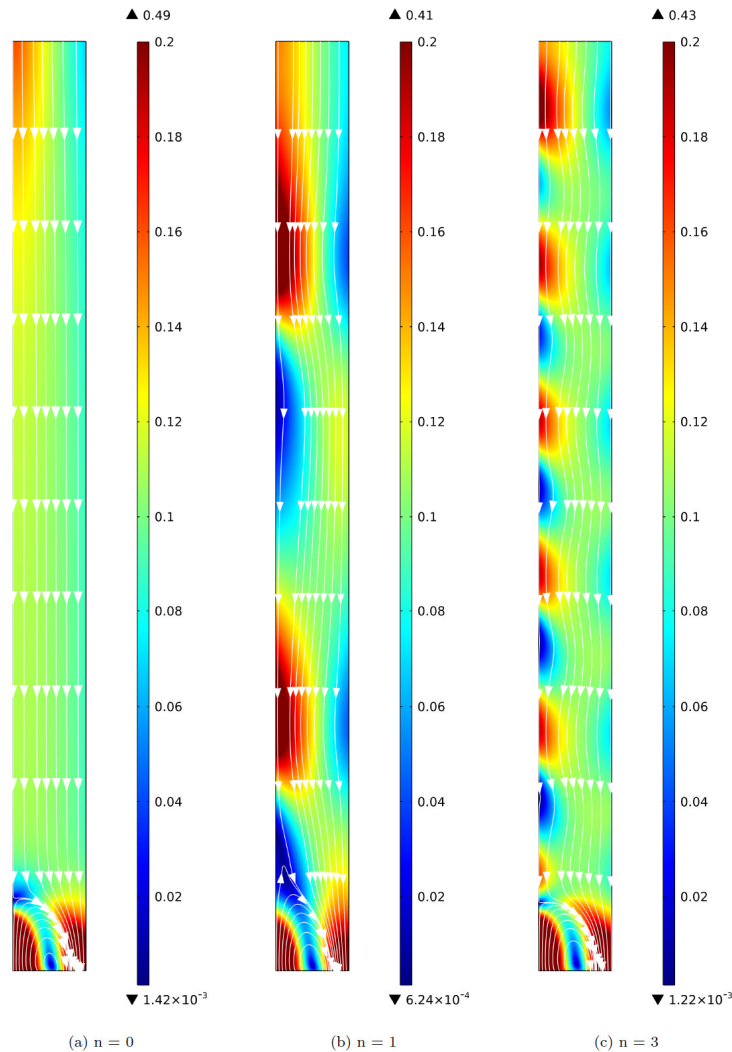


Fig. 9. The periodic dustcake ($h = 1 \text{ mm}$) induces an EHD flow showing characteristics of a wave-like flow field based on a discharge voltage of -25 kV and a mean velocity of 0.1 m s^{-1} .

3.6 Varying dustcake resistivity effect on particle trajectory under maximum charging

The formation of heterogeneous dustcake induces a flow field with wave-like streamlines that can alter the total trajectory length of charged particles during electrostatic precipitation. The integrated particle trajectory length at collection is an important property, as it can be used to infer the removal of total amount of gaseous mercury before the injected sorbent particles are collected by an ESP. A longer particle trajectory length for a given PAC size implies a longer resident time in an ESP for enhanced in-flight adsorption of gaseous mercury. In-flight adsorption of gaseous mercury by sorbent suspensions has been identified as one of the important mechanisms that promotes mercury removal [39, 40].

Fig. 10 and Fig. 11 show the integrated particle trajectory length of fly ash and PAC over hypothetical dustcake resistivity varying frequency (n) at particle collection. For each particle type, four particle fluxes each characterized by a constant mass flow rate of 1 mg s^{-1} (fly ash) and 0.1 mg s^{-1} (PAC) with particle diameters

ranging from 0.1 to 100 μm are introduced into the ESP with a background gas velocity of 0.1 m s^{-1} . The model particles are under maximum particle charging if they are introduced into the ESP near the discharge electrode. For both particle types under maximum charging, submicron particles having particle diameters of 0.1 and 1 μm have longer particle trajectory lengths than supermicron particles with 10 and 100 μm . This is mainly because field charging is the predominant charging mechanism when a particle flux is closer to the discharge electrode. This allows faster charging for the supermicron particles and shortened particle trajectory lengths. In comparison, submicron particles have longer particle trajectory lengths because of smaller saturation charges that enable the submicron particles to remain suspended for an extended period.

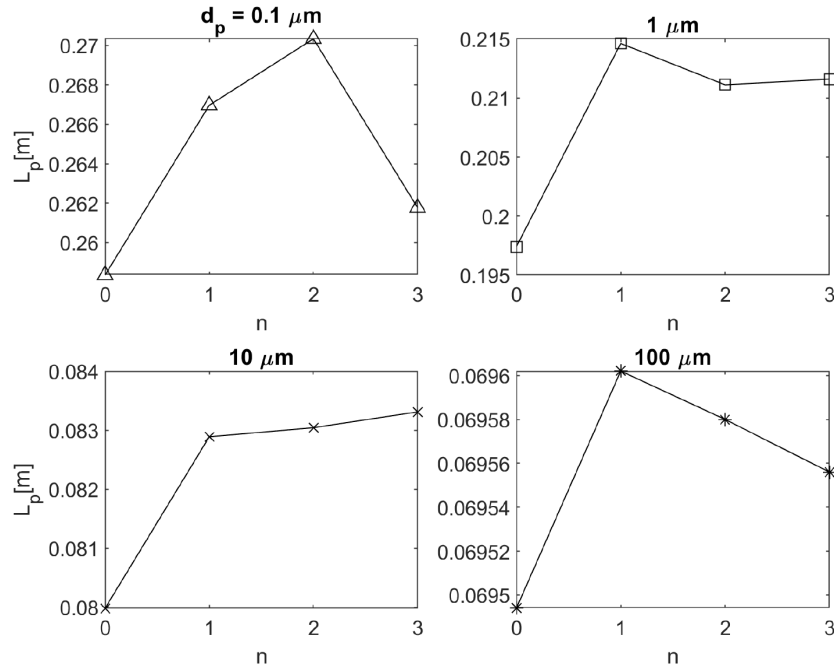


Fig. 10. Total simulated particle trajectory length at particle collection of four fly ash particle fluxes with particle diameters equal to 0.1, 1, 10, and 100 μm , which are fed into the ESP near the discharge electrode under maximum particle charging and a mean gas velocity of 0.1 m s^{-1} .

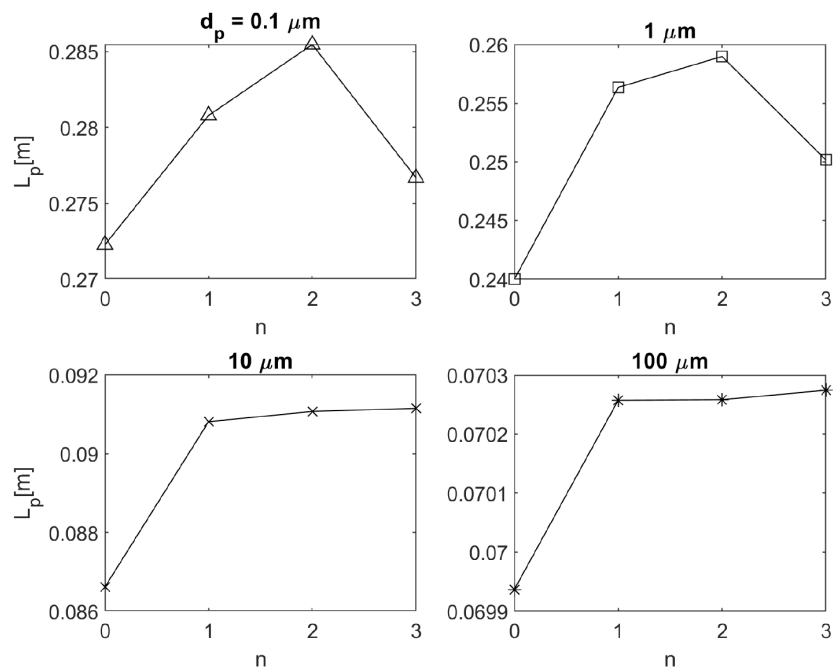


Fig. 11. Total simulated particle trajectory length at particle collection of four PAC particle fluxes with particle diameters equal to 0.1, 1, 10, and 100 μm that are fed into the ESP near the discharge electrode under maximum particle charging.

For both fly ash and PAC under maximum charging, increasing n in dustcake limits the total particle trajectory length of all tested particles. The effect is evidently clear for submicron particles of 0.1 and 1 μm . For PAC experiencing maximum charging (Fig. 11), the particle trajectory of $d_p = 0.1 \mu\text{m}$ first increases to a maximum value at $n = 2$ and decreases afterward showing a convex trend. For the case of supermicron particles of $d_p = 10$ and 100 μm , the total particle trajectory reaches a plateau as n increases. One possible explanation for this convex trend exhibited by submicron PAC is because as n is increased, it generates two effects in dustcake: First, increase in heterogeneity when the resistivity changes less frequently and second, decrease in heterogeneity when the resistivity changes more frequently. The second effect ultimately leads to the gradual transition from heterogeneous ($n = 1$ or 2) back to less heterogeneous ($n = 3$ and greater) simulating a homogeneous dustcake when n is zero.

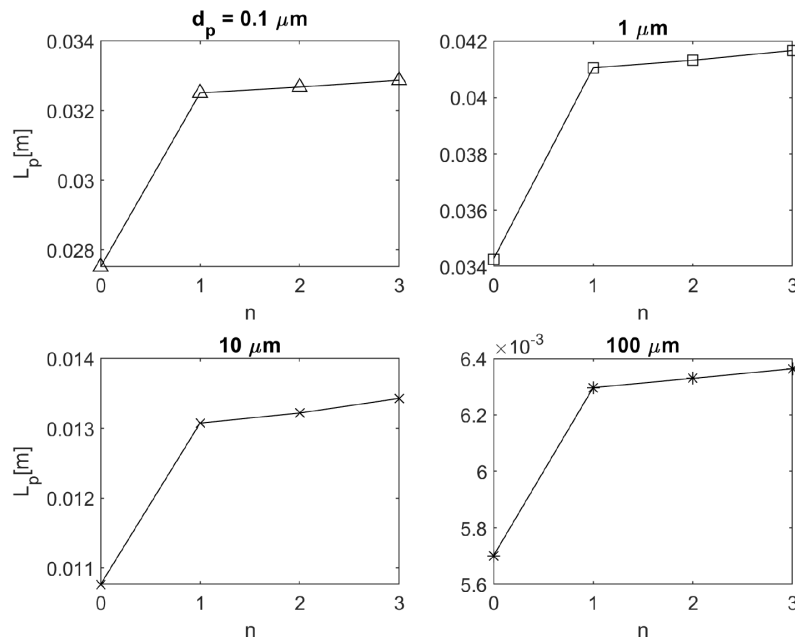


Fig. 12. Model-predicted integrated particle trajectory length at particle collection of four fly ash particle fluxes with particle diameters equal to 0.1, 1, 10, and 100 μm that are fed into the ESP near the collection electrode under minimum particle charging.

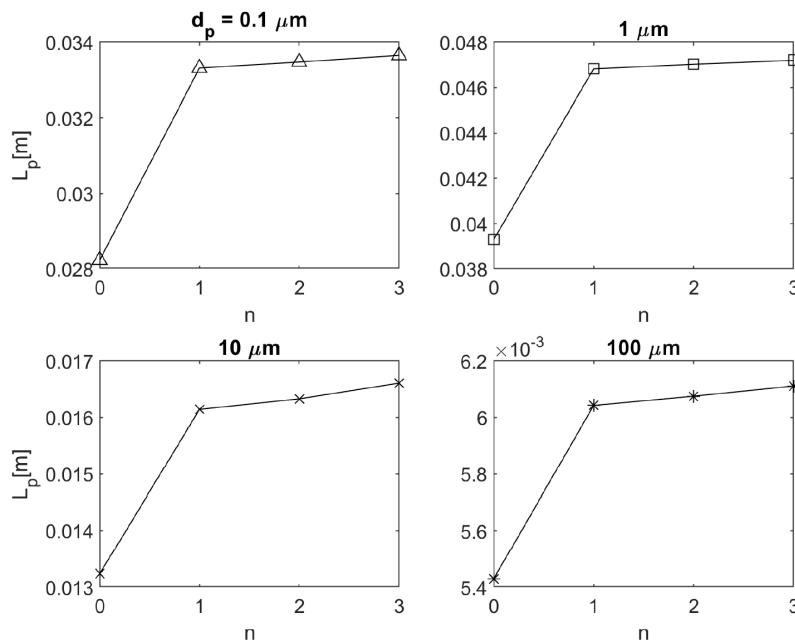


Fig. 13. Model-predicted integrated particle trajectory length at particle collection of four PAC particle fluxes with particle diameters equal to 0.1, 1, 10, and 100 μm that are fed into the ESP near the collection electrode under minimum particle charging.

3.7 Varying dustcake resistivity effect on particle trajectory under minimum charging

Fig. 12 and Fig. 13 show the model-predicted effect of heterogeneous dustcake resistivity on the integrated particle trajectory length of fly ash and PAC respectively under minimal particle charging. Near the surface of collection electrode, the particle charging field and ion density are minimal because this is the radial position farthest from the discharge electrode. In Fig. 12, the 1 μm fly ash particle has the longest particle trajectory length of all particle sizes reaching a metastable length as n increases. In comparison, PAC exhibits a similar trend, but the 1 μm PAC particle travels approximately 13% longer than the 1 μm fly ash particle. Under minimal particle charging, the 0.1 μm PAC particle only travels 2.4% longer than the 0.1 μm fly ash particle, mainly due to the additional charges acquired by the submicron particles through diffusion charging (i.e., R_d). Compared with the particles that experience maximum particle charging, the minimal charged particles do not necessarily travel the longest because these particles are also closest to the collection electrode, leading to shorter particle trajectory length and less frequent activities with gaseous mercury in the region near the boundary layer.

3.8 Varying dustcake resistivity effect on PAC charging

It has been shown that PAC travels a longer distance than coal fly ash at particle collection during the process of electrostatic precipitation. This is because PAC is non-spherical and has a smaller density and a lower relative permittivity than fly ash. As a result, the discussion herein focuses on the characterization of particle migration and collection of PAC. In an ESP, field charging is the predominant particle charging mechanism, which depends on the saturation charge and the local electric field strength. The presence of a heterogeneous resistivity dustcake can affect the charging of PAC because the particle charging field near the collection electrode is perturbed and the particle migration behaviors can be affected.

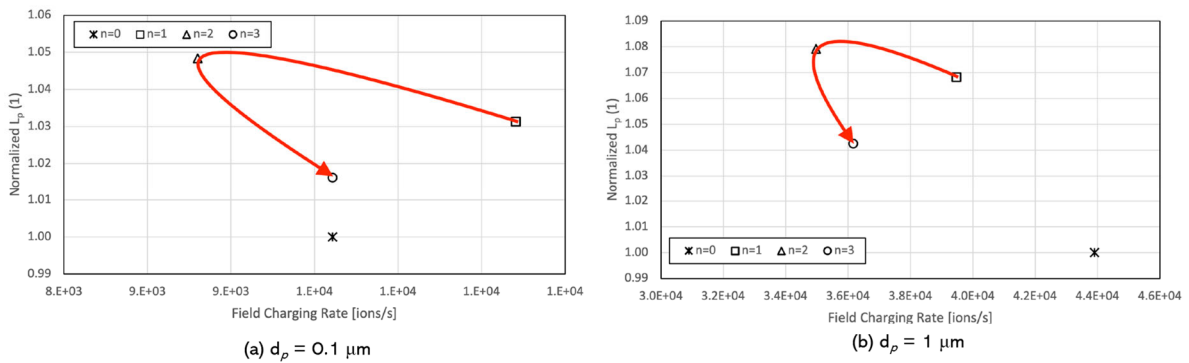


Fig. 14. Normalized integrated particle trajectory length over field charging rate (ions s^{-1}) of smaller PAC particles under maximum particle charging for various forms of heterogeneous resistivity dustcake defined by n with the increasing trend in n indicated by the red arrow: (a) $d_p = 0.1 \mu\text{m}$ and (b) $d_p = 1 \mu\text{m}$.

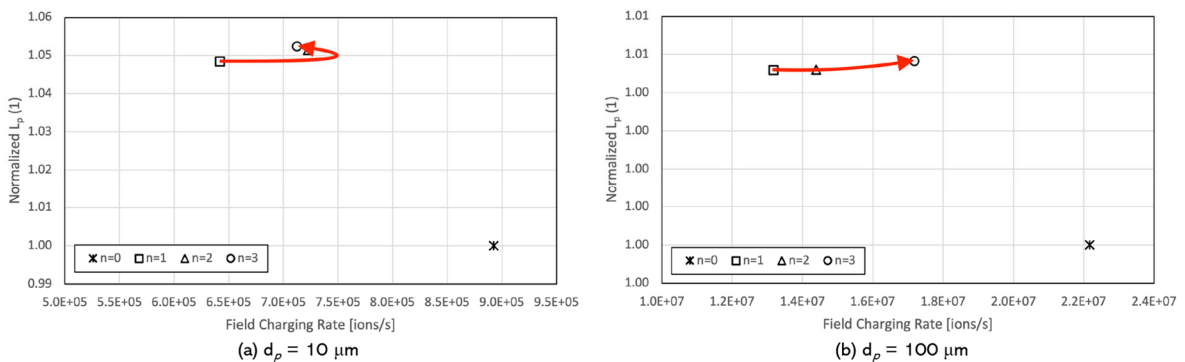


Fig. 15. Normalized integrated particle trajectory length over field charging rate (ions s^{-1}) of larger PAC particles under maximum particle charging for various forms of heterogeneous resistivity dustcake defined by n with the increasing trend in n indicated by the red arrow: (a) $d_p = 0.1 \mu\text{m}$ and (b) $d_p = 1 \mu\text{m}$.

Fig. 14 and Fig. 15 show the normalized integrated particle trajectory length (L_p) over field charging rate (Eq. 9) under maximum particle charging in terms of various hypothetical heterogeneous resistivity dustcake. The data point indicated by the symbol of asterisk represents the homogeneous dustcake ($n = 0$) and the symbols of square, triangle, and circle represent the cases of heterogeneous resistivity dustcake with n equals to 1, 2, and 3 respectively. In general, the increase in field charging rate in ions s^{-1} when coupled with 440 heterogeneous resistivity dustcake results in greater integrated particle trajectory lengths regardless of the value of n as compared with a homogeneous dustcake.

For $d_p = 0.1 \mu m$, in Fig. 14 (a), the increase is approximately 3% ($n = 1$), 5% ($n = 2$), and 2% ($n = 3$). For $d_p = 1 \mu m$, in Fig. 14 (b), the increase is approximately 7% ($n = 1$), 8% ($n = 2$), and 4% ($n = 3$). The normalized particle trajectory length follows a nonlinear trend over field charging rate and values of n . A higher value of n does not increase the particle trajectory length significantly and this could be because increasing the value of n results in a heterogeneous resistivity dustcake having electrical properties converged toward a homogeneous dustcake. In Fig. 14 (a), $n = 1$ represents an optimal case for $d_p = 0.1 \mu m$, because the particle flux travels 3% longer under a relative smaller field charging rate as compared with the case of a homogeneous dustcake. In Fig. 14 (b), longer particle trajectory lengths are achievable for different heterogeneous dustcake by using lower particle charging when compared with a homogeneous dustcake. The presence of a heterogeneous dustcake can likely lead to less energy consumption of an ESP when considering smaller particles.

In Fig. 15, for larger PAC particles ($d_p = 10$ and $100 \mu m$), the integrated particle trajectory length (L_p) becomes more predictable under the influence of heterogeneous resistivity dustcake. For $d_p = 10 \mu m$, the L_p increases asymptotically as n increases and the particle requires smaller field charging rate to reach a greater L_p . Based on Fig. 15 (a), the L_p of PAC with a d_p of $10 \mu m$ can potentially be increased by approximately 5% under the influence of heterogeneous dustcake. To a lesser degree, in Fig. 15 (b), the PAC with a diameter of $100 \mu m$ can also extend its L_p by approximately 1% under the influence of the heterogeneous dustcake, but it requires a higher field charging rate to achieve this increment in L_p as indicated in the Figure. Overall, the increase in L_p is limited for larger PAC particles because they can be charged more readily in a shorter period of time due to larger saturation charge. In addition, a lower field charging rate is required to achieve an increase in particle trajectory length under the influence of heterogeneous dustcake.

In the present study, a one-stage cylindrical ESP is modeled and field charging is known to be the dominant charging mechanism [11, 38]. As a result, the contribution from diffusion charging on particle suspensions is expected to be minimal. Fig. 16 and Fig. 17 show the normalized integrated particle trajectory length (L_p) over diffusion charging rate (ions s^{-1}). As shown in both Figures, it is evident that PAC particles receive fractional charges through diffusion charging. With respect to smaller PAC particles, the diffusion charging rate for $0.1 \mu m$ PAC centers around $1 \text{ ions } s^{-1}$ as the dustcake resistivity varies (Fig. 16 (a)), whereas for $1 \mu m$ PAC, the diffusion charging rate centers around $0.01 \text{ ions } s^{-1}$ (Fig. 16 (b)) as dustcake varying frequency (n) increases.

Based charging kinetics in ESPs [11], the charge received by larger PAC particles approaches zero as particle diameter increases and the role of heterogeneous dustcake becomes limited with respect to diffusion charging.

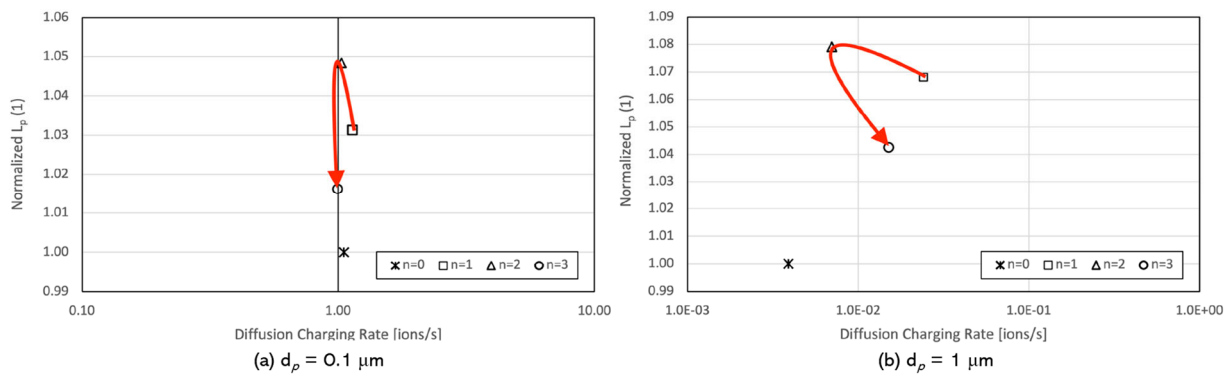


Fig. 16. Normalized integrated particle trajectory length over diffusion charging rate (ions s^{-1}) of smaller PAC particles under maximum particle charging for various forms of heterogeneous resistivity dustcake defined by n with the increasing trend in n indicated by the red arrow: (a) $d_p = 0.1 \mu m$ and (b) $d_p = 1 \mu m$.

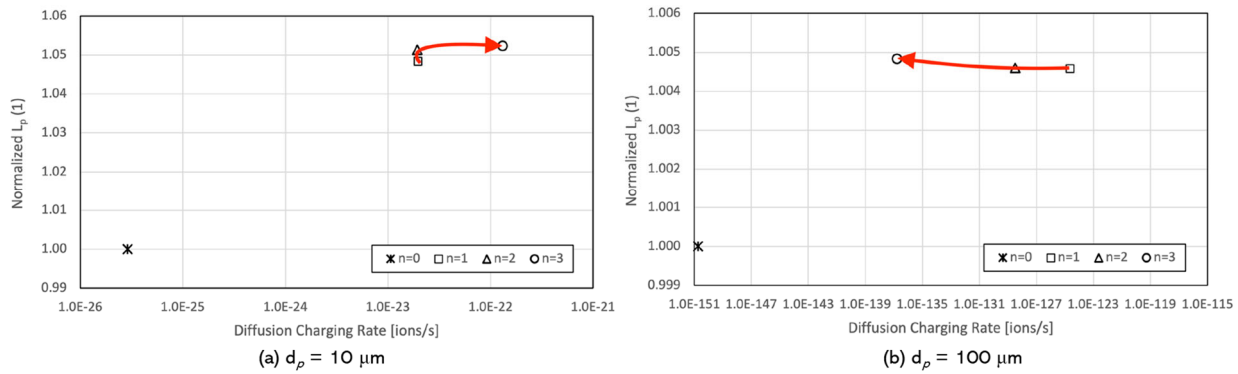


Fig. 17. Normalized integrated particle trajectory length over diffusion charging rate (ions s^{-1}) of larger PAC particles under maximum particle charging for various forms of heterogeneous resistivity dustcake defined by n with the increasing trend in n indicated by the red arrow: (a) $d_p = 10 \mu m$ and (b) $d_p = 100 \mu m$.

As particle diameter increases, larger particles obtain electric charges primarily through field charging in an ESP and only very small fractional charges are received through diffusion charging for supermicron particles as indicated in Fig. 17. As indicated by the charging theory (Eq. 10), the rate of diffusion charging decreases exponentially as particle diameter increases. Fig. 17 shows the normalized L_p over diffusion charging rate. It is evident that diffusion charging rates for both supermicron particles approaches zero. For $10 \mu m$ PAC particles, the increase in integrated particle trajectory is approximately 5% regardless of the values of n and the corresponding diffusion charging rate is in the order of 10^{-22} ions s^{-1} . In comparison, for $100 \mu m$ PAC particles, the increase in integrated particle trajectory is only 0.5% and the corresponding diffusion charging rate is in the order of 10^{-131} ions s^{-1} . Evidently, both diffusion charging rate and heterogeneous dustcake play a negligible role with respect to the integrated particle trajectory. This is because larger PAC particles receive a large number of ions and are collected by the electric field in a short period of time.

3.9 Effect of varying dustcake resistivity on particle collection efficiency

To study the differential collection behaviors between fly ash and PAC as a result of the oscillatory dustcake, the collection electrode are divided into three sections with the surface of the first collection electrode indicated in green color in Fig. 18. In the present modeling study, the background flow velocity is set to $0.1 m s^{-1}$, which always leads to a 100% particle collection efficiency. This is to study the distribution of the two particle types on the collection electrodes. Fig. 19 and Fig. 20 show the particle collection efficiencies of fly ash and PAC, respectively, in the first collection field of the cylindrical ESP as a function of particle diameters for different dustcake varying frequency (n).

In Fig. 19, the collection efficiency of fly ash shows a clear reduction in the first collection field. Overall, distribution of the reduction in collection efficiency is weakly lognormally shaped skewed toward the smaller particle sizes of fly ash. In a homogeneous dustcake when $n = 0$, the collection efficiency reaches a minimum of 80% for a particle size at approximately $0.25 \mu m$. As n increases, the standard deviation of the lognormally shaped distribution increases or the distribution widens. In Fig. 19, the rate of increase in standard deviation gradually decreases over n , which implies that the effect of oscillatory dustcake on fly ash collection becomes less significant at higher n values. Fly ash is more resistive with a higher saturation charge, so its particle collection is less affected by the oscillatory dustcake.

The collection of PAC is essential because PAC adsorbs gaseous mercury and the emissions of PAC can potentially lead to negative health effects after long periods of exposure to PAC suspensions. In Fig. 20, the collection efficiency of PAC follows a similar reduction distribution to fly ash except when the distribution has a larger standard deviation and the minimum collection efficiencies for the submicron particles are lower. The minimum PAC collection efficiency is $\sim 75\%$ for particle sizes ranging between 0.3 and $0.5 \mu m$. Compared with fly ash, the initial distribution of reduction in PAC collection efficiency ($n = 0$) also appears to have larger standard deviation. Increasing n further widens the distribution, indicating that more submicron PAC particles are not collected in the first collection field as the change in dustcake resistivity becomes more frequent. The corresponding averaged particle diameter with respect to the minimum particle collection efficiency is approximately $0.3 \mu m$ for fly ash and is approximately $0.4 \mu m$ for PAC considering all dustcake types. This

result agrees with the literature, which states that combined particle charging can result in a minimum electrical mobility for particles around $0.3 \mu\text{m}$ [38].

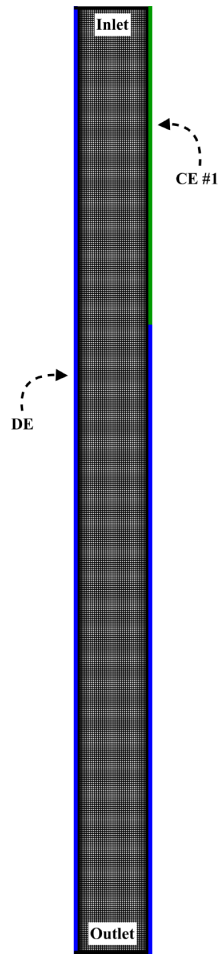


Fig. 18. The first collection electrode (CE) is indicated by the edge marked in green, where the discharge electrode (DE) is on the left of the axisymmetric domain.

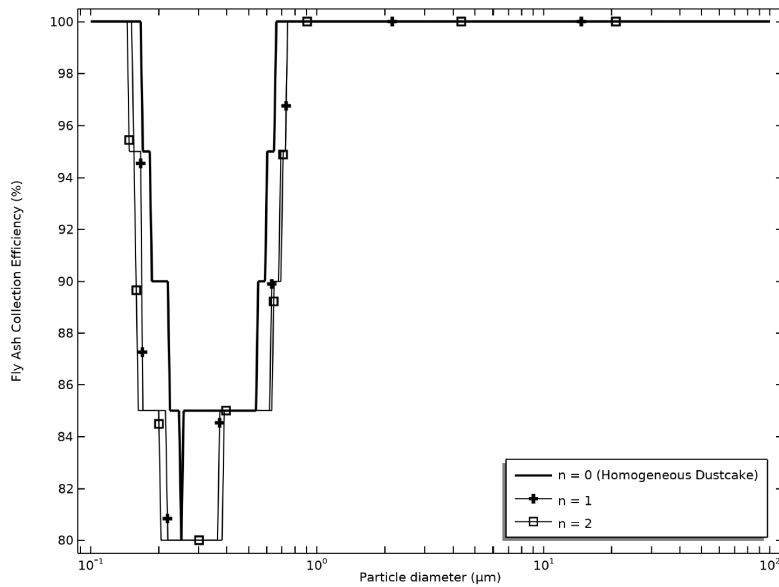


Fig. 19. The collection efficiency of fly ash (FA) for various dustcake resistivity varying frequencies with respect to the first CE of the cylindrical ESP.

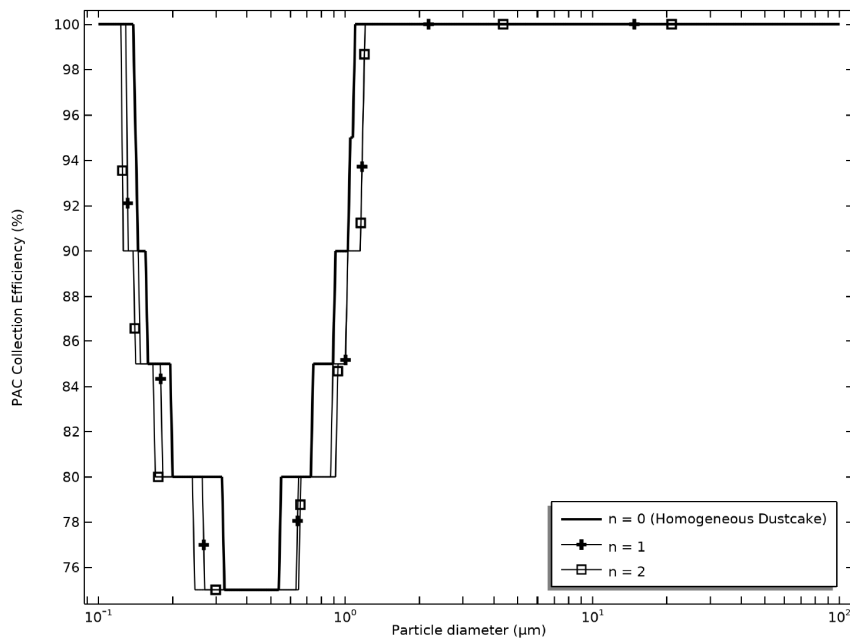


Fig. 20. The collection efficiency of PAC for various dustcake resistivity varying frequencies with respect to the first CE of the cylindrical ESP..

6. Conclusion

Based on the qualitative results from our previous experimental study [5], a numerical model was developed in COMSOL Multiphysics® to conduct a case study centering on the effect of heterogeneous dustcake on the particle charging and collection of fly ash and PAC in a cylindrical ESP. The heterogeneous dustcake was modeled by an oscillatory cosine function with powder resistivity varying spatially along the collection electrode defined by different dustcake varying frequencies (n). Assuming a mean gas velocity of 0.1 m s^{-1} through a 2-D axisymmetric domain, the numerical results due to the presence of a heterogeneous dustcake are summarized as the following.

The electric field is perturbed near the collection electrode surface, leading to distorted electric field lines that can alter the particle trajectories near the surface of collection electrode. A 2-D distribution of ion density is induced with the number of localized maximum increases in the inter-electrode space as the dustcake varying frequency (n) increases. The induced EHD flow exhibits wave-like flow characteristics because of the oscillatory dustcake. Under the maximum rate of particle charging, the wave-like EHD flow, which enables PAC to travel longer distances than fly ash at particle collection, and the particle trajectory length of both particles depends on n . Under the minimum rate of particle charging, the particle trajectory length of all tested particles reaches a local maximum at $n = 1$ but continues to increase asymptotically as n increases. Varying dustcake resistivity can lead to increases in the integrated particle trajectory lengths for all tested particles regardless of rate of field charging, the dominant charging mechanism in ESPs. In some cases, increases in the particle trajectory lengths can be achieved with lower than the field charging rate of homogeneous dustcake ($n = 0$) for enhanced mass transfer between gaseous mercury and PAC. Based on the collection efficiency in the first collection field (Fig. 18), increasing n widens the distribution of uncollected particles for both fly ash and PAC. Future studies will center on experimentally mapping the distribution of PAC along the collection electrode and experimentally exploring the migration behaviors near the collection electrode under the influence of an oscillatory dustcake. The induced wave-like EHD flow can likely lead to particle penetration through ESPs.

Acknowledgment

Both authors would like to express their gratitude for the computational resources provided by Northern Illinois University (NIU) and University of Michigan to make this modeling study possible.

References

- [1] Brown T.D., Smith D.N., Hargis Jr. R.A., and O'Dowd W. J., Mercury measurement and its control: What we know, have learned, and need to further investigate., *J. Air & Waste Manage. Assoc.*, Vol. 49 (6), pp. 1–97, 1999.
- [2] Pavlish J.H., Field testing of activate carbon injection options for Hg control at TXU's Big Brown station, in: Power Plant Pollutant Control MEGA Symposium, 2006.
- [3] Sjostrom S., Ebner T., Ley T., Slye R., Richardson C., Machalek T., Richardson M., and Chang R., Assessing sorbents for mercury control in coal-combustion flue gas, *J. Air & Waste Manage. Assoc.*, Vol. 52 (8), pp. 902–911, 2002.
- [4] Dombrowski K., Mercury control for plants ring texas lignite and equipped with ESP- wet FGD, Tech. rep., URS Group, Inc., March 2010.
- [5] Lee E.M., and Clack H.L., Powder resistivity inferred differential collection of heterogeneous coal fly ash and powered activated carbon admixtures within a cylindrical electrostatic precipitator, *Emiss. Coltrol Sci. Technol.*, Vol. 2 (1), pp.33–43, 2016.
- [6] Chang C.L., and Bai H.L., An experimental study on the performance of a single discharge wire-plate electrostatic precipitator with back corona, *J. Aerosol Sci.*, Vol. 30 (3), pp. 325–340, 1999.
- [7] Jaworek A., Czech T., Rajch E., and Lackowski M., Laboratory studies of back-discharge in fly ash, *J. Electrostat.*, Vol. 64 (5), pp. 306–317, 2006.
- [8] Czech T., Sobczyk A.T., Jaworek A., and Krupa A., Corona and back discharges in flue-gas simulating mixture, *J. Electrostat.*, Vol. 70 (3), pp. 269–284, 2012.
- [9] Ni M., Yang G., Wang S., Wang X., Xiao G., Zheng C., Gao X., Luo Z., and Cen K., Experimental investigation on the characteristics of ash layers in a high-temperature wire-cylinder electrostatic precipitator, *Sep. Purif. Technol.*, Vol. 159, pp. 135–146, 2016.
- [10] Krupa A., Podlinacuteski J., Mizeraczyk J., and Jaworek A., Velocity field of EHD flow during back corona discharge in electrostatic precipitator, *Powder Technology (Netherlands)*, Vol. 344, pp. 475–486, 2019.
- [11] Lawless P.A., and Sparks L.E., Modeling particulate charging in ESPs, *IEEE Trans. Ind. Applicat.*, Vol. 24 (5), pp. 922–927, 1988.
- [12] Hoburg J.F., Charge-density, electric-field, and particle charging in electrostatic precipitation with back ionization, *IEEE Trans. Ind. Applicat.*, Vol. 18 (6), pp. 666–672, 1982.
- [13] Penney G.W., Hewitt, Jr. J.G., Some measurements of abnormal corona, *Trans. AIEE, Part 1 Commun. Electron.*, Vol. 77 (3), pp. 319–327, 1958.
- [14] Bacchiega G., Gallimberti I., Sani E., Sala R., Arrondel V., Hamlil M., and Christensen E., Experimental study of the mass balance in a pilot industrial electrostatic precipitator, *J. Electrostat.*, Vol. 64 (5), pp. 277–289, 2006.
- [15] Ivancsy T., Kiss I., and Berta I., Improved model for the analysis of back corona in pulse energised electrostatic precipitators, *J. Electrostat.*, Vol. 67 (2–3), pp. 146–149, 2009.
- [16] Jansky J., Gaychet S., Bessieres D., Soulem N., Paillol J., and Lemont F., Numerical simulation of back discharge ignition, *J. Phys. Appl. Phys.*, Vol. 47 (6), 065202, 2014.
- [17] Lee E. M., Clack H. L., Multiscale modeling of electrostatic precipitations of fly ash and mercury sorbents: Discontinuous current density effects, *Int. J. Multiphase Flow*, Vol. 146, 103877, 2022.
- [18] Gao W., Wang Y., Zhang H., Guo B., Zheng C., Guo J., Gao X., and Yu A., A numerical investigation of the effect of dust layer on particle migration in an electrostatic precipitator, *Aerosol and Air Qual. Res.*, Vol. 20 (1), pp. 166–179, 2020.
- [19] Zheng C., Zhang H., Liu X., Wang Y., Gao W., Zheng H., Sun D., and Gao X., Effect of dust layer in electrostatic precipitators on discharge characteristics and particle removal, *Fuel*, Vol. 278, 118335, 2020.
- [20] Zhang H., Wang Y., Gao W., Wu Z., Yang Z., Yang Y., Wu W., Zheng C., and Gao X., Minimizing the adverse effects of dust layer on the particle migration in electrostatic precipitator under various temperature, *Fuel Processing Technol.*, Vol. 213, 106659, 2021.
- [21] COMSOL Multiphysics®, Stockholm, Sweden, Particle Tracing Module User's Guide, Vol. 5.6 Edition (2021).
- [22] Ramechecandane S., Beghein C., Eswari N., Modeling particulate removal in plate-plate and wire-plate electrostatic precipitators., *Int. J. Multiphysics*, Vol. 8 (2), pp. 145–168, 2014.
- [23] Lawless P. A., and Sparks L. E., A mathematical model for calculating effects of back corona in wire-duct electrostatic precipitators, *J. Appl. Phys.*, Vol. 51 (1), pp. 242–256, 1980.
- [24] Zhang J., Du Y., Wu H., Pan W., Ren J., and Hu D., Numerical study on PM10 collection efficiency in a wire-cylinder electrostatic precipitator under multi-field coupling., *Int. J. Environ. Stud.*, Vol. 71 (3), pp. 344–359, 2014.
- [25] Davidson J. H., and Shaughnessy E. J., Turbulence generation by electric body forces, *Exp. Fluids*, Vol. 4 (1), pp. 17–26, 1986.
- [26] Bottner C.U., The role of the space charge density in particulate processes in the example of the electrostatic precipitator, *Powder Technol.*, Vol. 135, pp. 285–294, 2003.
- [27] Schmid H.J., On the modelling of the particle dynamics in electro-hydrodynamic flow fields: II. Influences of inhomogeneities on electrostatic precipitation, *Powder Technol.*, Vol. 135 (SI), pp. 136–149, 2003.

- [28] Farnoosh N., Adamiak K., and Castle G.S.P., 3-D numerical simulation of particle concentration effect on a single-wire esp performance for collecting poly-dispersed particles, *IEEE Trans. Dielectr. Electrical Insul.*, Vol. 18 (1), pp. 211–220, 2011.
- [29] Lei H., Wang L.Z., and Wu Z.N, EHD turbulent flow and Monte-Carlo simulation for particle charging and tracing in a wire-plate electrostatic precipitator, *J. Electrostat.*, Vol. 66 (3–4), pp. 130–141, 2008.
- [30] COMSOL Multiphysics, Introduction to Particle Tracing Module, Version 5.2 Edition, 2015.
- [31] Kaptsov N. A., *Elektricheskie Inventiia v Gazakh I Vakuume*, Ogiz, Moscow, U.S.S.R., pp. 587–630, 1947.
- [32] Lee E. M., Impact of powder heterogeneity on particle collection behaviors in a cylindrical electrostatic precipitator, Ph.D. thesis, Illinois Institute of Technology, 2019.
- [33] Sjöholm P., Ingham D.B., Lehtimäki M., Perttu-Roiha L., Goodfellow H., and Torvela H., Gas cleaning technology (Chapter 13), in: *Industrial Ventilation Design Guidebook*, Academic Press, 2001.
- [34] Kunii D., Levenspiel O., *Fluidization Engineering*, second edition Edition, Butterworth-Heinemann, Boston, MA, 1991.
- [35] Raghavendra S.C., Raibagkar R.L., and Kulkarni A.B., Dielectric properties of fly ash, *Bull. Mater. Sci.*, Vol. 25 (1), pp. 37–39, 2002.
- [36] Hotta M., Hayashi M., Lanagan M.T., Agrawal D.K., and Nagata K., Complex permittivity of graphite, carbon black and coal powders in the ranges of x-band frequencies (8.2 to 12.4 GHz) and between 1 and 10 GHz, *ISIJ International*, Vol. 51 (11), pp. 1766–1772, 2011.
- [37] Ristenpart W., Jiang P., Slowik M., Punckt C., Saville D., and Aksay I., Electrohydrodynamic flow and colloidal patterning near inhomogeneities on electrodes, *Langmuir*, Vol. 24 (21), pp. 12172–12180, 2008.
- [38] Hinds W. C., *Aerosol technology: Properties, behavior, and measurement of airborne particles*, 2nd Edition, Wiley-Interscience, 1999.
- [39] Clack H. L., Simultaneous removal of particulate matter and gas-phase pollutants within electrostatic precipitators: Coupled in-flight and wall-bounded adsorption, *Aerosol and Air Quality Res.*, Vol. 15 (6), pp. 2445–2455, 2015.
- [40] Clack H.L., Numerical simulation of simultaneous electrostatic precipitation and trace gas adsorption: Electrohydrodynamic effects, *Frontiers in Energy Research* 5, 2017.